Speckle Photometry and Spectral Types of Close Binary Star Components

Rick Wasson[1], Russell Genet[2], and Dave Rowe[3]

[1]Orange County Astronomers, Murrieta, California, ricksshobs@verizon.net
[2]California Polytechnic State University, Payson, Arizona
[3]PlaneWave Instruments, Adrian, Michigan

Abstract

Relatively few visual binary stars in the Washington Double Star (WDS) Catalog have spectral types given for both components. A speckle photometry method for observation of close binaries is presented which simultaneously measures orbital position, derives color indices, and estimates spectral types of the individual stellar components. The method combines the techniques of speckle interferometry for diffraction-limited astrometry, bispectrum analysis for relative flux distribution of the two components, and an adaptation of differential photometry for photometric calibration. Observations in multiple Sloan filter bands - together with a simple method for approximate photometric transformation to standard Sloan magnitudes - yield color indices which are correlated with spectral type. Measured astrometry, Sloan magnitudes, color indices and spectral types of the individual binary components are presented and discussed, as well as the within-night and night-to-night variations and error sources. The observations were made remotely with the Fairborn Institute Robotic Observatory's 11-inch telescope.

1. Introduction

Speckle interferometry and Bispectrum analysis have become standard techniques used by professional astronomers for astrometric observation of visual binary stars to measure orbits and determine stellar masses and ages (Davidson et al. 2009). Measurement of color indices and corresponding spectral types of the individual components can provide useful supplementary information to support binary orbit solutions and more accurate definition of stellar masses and other properties for both the individual components and the total binary system (McAlister 1985, and Horch et al. 2001, 2004 and 2006).

Over the last decade, one of us (DR) has developed free Windows-based software packages that enable amateurs and students to conduct speckle interferometric observations of double stars with small telescopes. These programs make it easy to find appropriate targets in the Washington Double Star Catalog (WDS) (Rowe 2017) and in the Gaia DR2 database (Rowe 2018); perform speckle autocorrelation analysis (Rowe & Genet 2015 and Harshaw, Rowe & Genet 2017); and explore bispectrum analysis (Rowe 2020).

In 2020, one of us (RG) completed building a remotely accessible observatory for speckle observations by students and amateur mentors. Several teams have already made observations and published papers (Marchetti et al. 2020, Caputo et al. 2020, Altunin et al. 2020, and Marchetti et al 2021). Additional papers are in publication.

The speckle photometry method presented here uses speckle interferometry for astrometry within the seeing disk (isoplanatic patch), bispectrum analysis (BSA) for flux proportions of the two stellar components, multi-band observations in Sloan filters, (a simple method for approximate photometric calibration), transformation of component magnitudes to the standard Sloan system, and color indices to estimate spectral types for the individual binary components. The method combines the techniques of speckle interferometry for diffraction-

limited resolution, with a modified version of differential photometry for photometric self-calibration. Speckle bispectrum analysis yields both astrometry and flux measurements.

The method described here may be applied to known or suspected visual binaries, many of which have long orbital periods that are poorly known. Identification of color indices and spectral types of the components may help improve orbit solutions and masses before a complete orbit has been observed.

A similar paper with the same observations was published previously (Wasson, Genet and Rowe, 2021). This paper has been reorganized, re-written with new analysis material, and shortened, to be more concise and easily available to double star observers.

2. Goals

The three main goals of this project were:
1. To explore the capabilities of speckle bispectrum analysis to measure photometrically the component magnitudes in several standard photometric bands.
2. To demonstrate whether color indices of the individual components could be measured with sufficient accuracy to estimate their spectral types.
3. To evaluate the uncertainties inherent in the method and identify the major sources of uncertainty.

3. Equipment

Observations were made with the Fairborn Institute Remote Observatory (FIRO) telescope shown in Figure 1 (Marchetti, Caputo, and Genet, 2020). The telescope consists of C-11 optics on a custom "L" mount driven by a SiTech control system (Gray 2020). Instrumentation consists of a ZWO ASI 1600MM CMOS camera, 1.5X Barlow lens, automated Clement focuser, and five-position filter wheel with Sloan filters: g', r', i', and z' (Generation 2 filters from Astrodon).

Figure 1. The FIRO robotic observatory was accessed remotely in real time for the observations described in this paper

The Astrodon filter characteristics, shown in Figure 2, were designed to match wavelengths of the Sloan Digital Sky Survey (SDSS) as closely as possible, but have higher transmission (up to 99%). The front-illuminated CMOS camera quantum efficiency (QE) declines earlier than the back-illuminated CCD detectors used in the SDSS. Therefore, the Astrodon z′2 long-pass filter was chosen to maximize sensitivity.

After these observations were made, the observatory was moved to a new home in Payson, Arizona, and the ZWO ASI 1600 camera was replaced with a ZWO ASI 183 camera that has a backside illuminated chip with higher QE, especially in the near infrared.

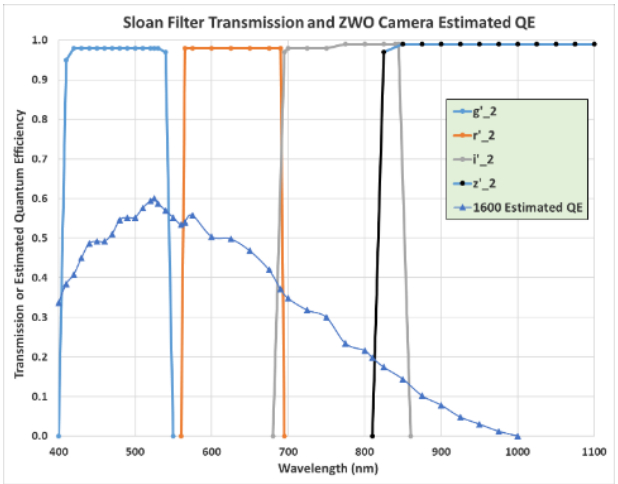

Figure 2A. The Astrodon filter set was used for all observations. Approximate filter characteristics and camera QE were derived from manufacturer's literature, with estimated peak QE = 60% for the front-illuminated CMOS detector. The z'_2 long-pass filter was used instead of z_s2 cutoff filter to maximize sensitivity.

Astrodon Filters with ZWO ASI 1600MM Camera	
Filter	**Convolved WL (nm)**
g'	485
r'	624
i'	758
z'	871

Figure 2B: Filter equivalent center wavelengths, convolved with the ZWO ASI 1600MM camera QE.

4. Target Selection

To develop and explore the potential of this method, the WDS Catalog was searched, using the WDS1.2 program (Rowe 2017) with the following search limits: 0.7"<ρ<3"; M_A<10; Dec>0; and Δmagnitude < 2. The four stars in Table 1 were selected for validation observations because they met the following criteria: they have orbit solutions and main sequence spectral types for both components given in WDS (verified in Simbad), their components sample a broad range of spectral types (A F G K M), and standard unresolved Sloan magnitudes were available from all-sky surveys. Orbit details were taken from the WDS 6th Orbit Catalog.

It is noted that the Hipparcos and Gaia satellites have already resolved these binaries and provided high-quality photometry for them. However, once validated with a small telescope, this method should enable speckle photometry with larger apertures that could reach smaller separations (and hence shorter periods), well below the ~0.6" Gaia resolution limit.

WDS Data for Binary Stars Observed						Gaia Data			
Coordinates	Discovery	Mag (V)	Ephemerides	Spec Type	Orbit Period	G	Bp-Rp	Parallax	Distance
		A	θ (deg)	A	(yr)	A	A	(mas)	(pcs)
		B	ρ (")	B		B	B		
22280+5742	KR 60AB	9.93	205.5	M3.5	44.58	8.641	2.692	249.68	4.01
		11.41	2.057	M4.5		9.911	2.914		
23050+3322	STF 2974AB	8.07	166*	A0V	None	8.044	0.061	4.07	245.7
		8.46	2.7*	A3V		8.384	0.251		
00014+3937	HLD 60	9.09	165.1	K0V	217.3	8.872	0.983	19.47	51.4
		9.77	1.329	K1V		9.395	1.196		
04301+1538	STF 554	5.7	15.1	F0V	172.5	5.591	0.413	21.03	47.6
		8.12	1.43	G0V		7.869	1.226		

* No orbit has been estimated for this long-period system. The values are the last reported in WDS (2016).

Table 1. Summary of characteristics of the four binary stars observed in this initial development of the Speckle Photometry method. The first 6 columns are from the WDS Catalog: WDS coordinates, Discovery code, magnitude (assumed to be V band), predicted θ and ρ on 2021.0 (from the 6th Orbit Catalog), WDS spectral type, and orbital period (6th Orbit Catalog). Supplementary data from the Gaia (DR2) catalog are also provided: Gaia(DR2) G magnitude, (Bp-Rp) color index, parallax (milli-arc-seconds), and distance (parsecs).

5. Astrometry Results

The binary stars were observed with normal speckle techniques, consisting of many short exposures (frames) for each filter. For example, 1000 exposures of 30 to 100 milli-seconds, in a small 256x256 pixels Region of Interest (ROI), were normally taken for each filter. A single Reference star, with the same exposures, ROI, and filter, was also observed; the reference star frames were used in deconvolution to remove optical aberrations that appear in both the binary and single star images.

Bispectrum Analysis, also known as triple correlation, was performed on the frames. BSA processing yields a reconstructed, diffraction-limited image of the binary star, from which astrometric measurements of separation and position angle are made. All speckle frames were analyzed using the BSA "tools" in the Speckle Tool Box (STB) software (Rowe 2020).
Calibration of image scale (arc-sec/pixel) and camera orientation on the sky was by plate solving several full-frame images of the area surrounding the target on each night. Plate solving is incorporated into the SiTech telescope control software, as well as the SiTech ZWOCam camera control software, and is the standard speckle calibration procedure at FIRO. Plate solving produces remarkably accurate and consistent calibration results, much better than the drift calibration method used in earlier speckle observations (Wasson 2019).

Astrometry results are summarized in Table 2. Several sets of filter sequences were repeated because photometry characteristics and uncertainties were being explored, as described in Section 6. Therefore, the astrometry also benefited from measurements in four filters and repeated in several "sets" noted in Table 2. Typical examples of BSA images are shown in Figure 3.

Calendar Date Bessel Date	WDS Discovery	Filter	θ Obs (deg)	σ(θ) (deg)	ρ Obs (arc-sec)	σ(ρ) (arc-sec)	Exposure (sec)	# Frames	# Sets
2020-10-20	22280+5742	g'	208.30	0.84	2.035	0.021	0.050	1000	5
2020.805	KR 60AB	r'	207.73	0.15	2.054	0.004	0.060	1000	5
		i'	207.84	0.21	2.039	0.029	0.080	1000	4
		z'	207.95	0.03	2.044	0.019	0.120	1000	5
	Overall Average ==>		208.00		2.043				
	Overall Std Deviation ==>		0.49		0.020				
2020-10-31	22280+5742	g'	209.03	2.28	2.067	0.073	0.060	1000	3
2020.835	KR 60AB	r'	207.53	0.54	2.089	0.012	0.080	1000	3
		i'	206.69	0.12	2.094	0.010	0.080	1000	3
		z'	206.87	0.25	2.070	0.015	0.150	1000	3
	Overall Average ==>		207.53		2.080				
	Overall Std Deviation ==>		1.39		0.035				
2020-12-04	22280+5742	g'	206.08	0.47	2.046	0.045	0.060	300	3
2020.928	KR 60AB	r'	206.32	0.48	2.055	0.019	0.060	300	3
		i'	206.81	0.03	2.056	0.010	0.080	300	3
		z'	206.59	0.08	2.052	0.013	0.150	300	3
	Overall Average ==>		206.45		2.052				
	Overall Std Deviation ==>		0.41		0.022				
2020-11-28	23050+3322	g'	166.29	0.15	2.676	0.004	0.020	1000	6
2020.912	STF 2974	r'	166.16	0.06	2.686	0.003	0.030	1000	6
		i'	166.14	0.07	2.687	0.004	0.080	1000	6
		z'	166.47	0.14	2.683	0.004	0.300	1000	6
	Overall Average ==>		166.27		2.683				
	Overall Std Deviation ==>		0.17		0.006				
2020-12-15	00014+3937	g'	163.17	1.03	1.354	0.006	0.030	500	4
2020.958	HLD 60	r'	164.64	0.79	1.351	0.008	0.040	500	4
		i'	165.69	1.05	1.352	0.030	0.080	500	4
		z'	165.64	0.54	1.359	0.008	0.300	500	2
	Overall Average ==>		164.66		1.353				
	Overall Std Deviation ==>		1.35		0.016				
2021-01-15	04301+1538	g'	14.58	0.74	1.509	0.012	0.020	1000	4
2021.041	STF 554	r'	15.35	0.55	1.524	0.025	0.030	1000	5
		i'	16.74	1.24	1.507	0.040	0.060	1000	5
		z'	14.65	1.00	1.468	0.023	0.100	1000	3
	Overall Average ==>		15.45		1.505				
	Overall Std Deviation ==>		1.23		0.032				
2021-02-06	04301+1538	g'	14.67	0.14	1.466	0.010	0.030	500	4
2021.101	STF 554	r'	14.49	0.33	1.436	0.023	0.030	500	4
		i'	15.54	0.96	1.416	0.026	0.060	500	4
		z'	14.56	1.25	1.424	0.036	0.200	500	4
	Overall Average ==>		14.82		1.435				
	Overall Std Deviation ==>		0.85		0.030				

Table 2. Summary of astrometric measurements. The columns are: date, WDS coordinates and discovery designation, Sloan filter, average position angle and standard deviation, average separation and standard deviation, speckle exposure time, number of speckle frames recorded in each set, and number of repeated sets of observations. For θ and ρ, the statistics are for the number of sets in each filter. For each star, the overall average and standard deviation, combining all filters and all sets of observations, are shown in yellow.

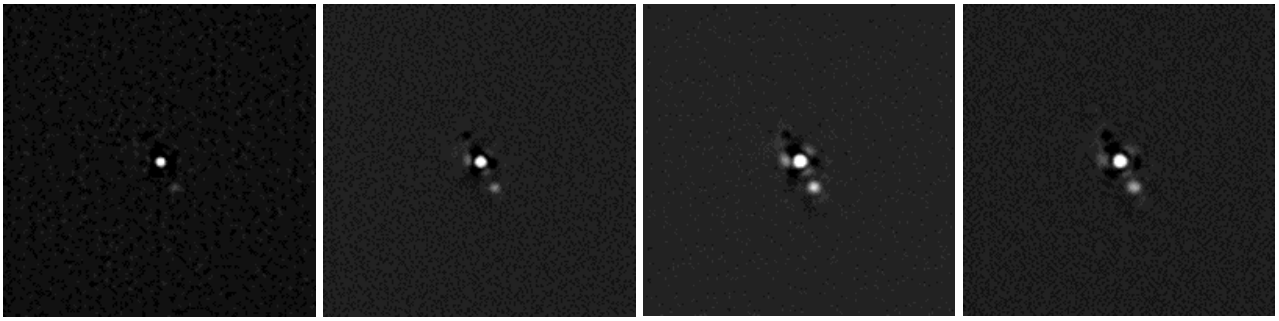

Figure 3. Bispectrum Region of Interest images from the first set of observations of KR60AB, with North up, East left. The images are 128x128 pixels (22"x22") in size. Left to right: Sloan g' r' i' z' bands. This red dwarf pair is relatively faint in g′ and even in r′, but is still bright in z′, even though camera QE has fallen off.

6. Speckle Photometry Overview

The speckle photometry method has nine major observation and data reduction steps which are summarized here and discussed in detail with example data in Section 7.

A. Observation
   1. Normal speckle observations
   2. Long exposures
   3. Reference star

B. Data Reduction and Analysis
   4. Astrometry
   5. Flux proportions
   6. Photometric self-calibration
   7. Component standard magnitudes
   8. Component color indices
   9. Component spectral types

The Speckle Photometry observation procedure is outlined in the flow diagram of Figure 4. One “set” of observations consists of a sequence of speckle frames immediately followed by a few long exposures, repeated for each of the four filters in the order shown.

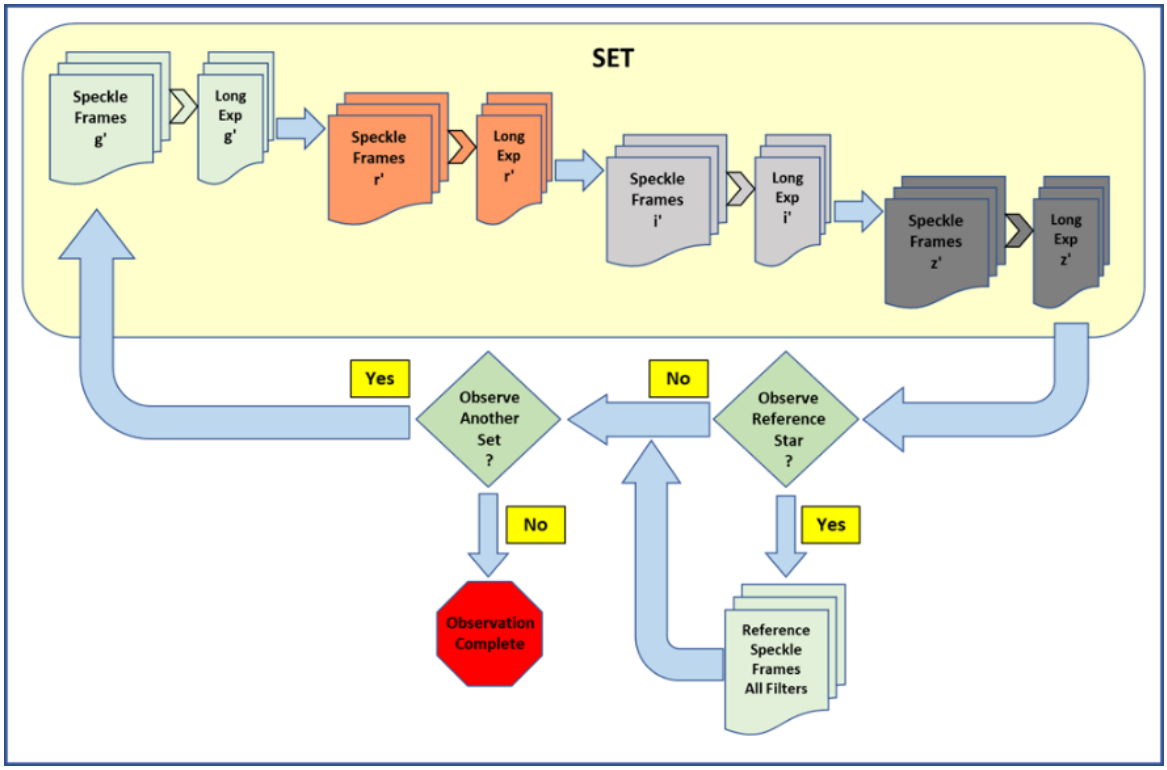

Figure 4. Flow Diagram of Speckle Photometry observation sequence.

The long exposures serve to calibrate the photometry, as explained in Sections 7.3 and 7.4. The filters are cycled rapidly within the set; after data processing, the filter sequence yields calibrated color indices within the set (Sections 7.5 and 7.6) that were taken as close together in time as possible. Three to six independent sets compose a single nightly observation, yielding repeatability statistics for the astrometric and photometric results.

The reference star, important for speckle quality, is generally observed near the middle of the sets to maximize the benefit to all the speckle data. The reference star is used in standard speckle deconvolution processing to normalize the effects of optical aberrations on spatial information in the speckle frames, sharpening the bispectrum image results. No long exposures are required for the reference star since it does not contribute photometric information.

7. Photometry Process Description

7.1 Normal Speckle Observations

The product of BSA processing of the large number of speckle frames for each filter is a single diffraction-limited image. Four measurements are extracted from a BSA image: astrometric θ and ρ measurements (Section 5), and photometric net flux ADU of each component star. The photometry results constitute the new method of this paper. Therefore, these procedures and results are discussed in more detail below.

STB processing from raw speckle frames to BSA diffraction-limited images was outlined in Section 5 for astrometry, where θ and ρ measurements were made by centroiding the star images in a separate circular aperture around each star. At the same time, the STB measurement tools also provide ADU flux within those apertures, the average background ADU from a third aperture, and the net flux for each star. Analysis of the STB BSA astrometry and photometry results for all the repeated "sets" of filters, were copied to a series of three Excel spreadsheets, along with significant observation and measurement parameters. The spreadsheets each deal with one of the major products of the investigation: speckle astrometry, photometry and color indices, and estimated component spectral types. These spreadsheets provided a convenient format for consistent data reduction, analysis, statistics, and plotting.

7.2 Flux Proportions

STB measurement tools use a set of circular apertures to measure the centroid positions of each star and to sum the ADU flux within the apertures. For astrometry, slightly different size apertures may be used with little effect on centroids. However, for photometry, it is critical that the same size apertures are used for both stars, thus measuring the same *proportion* of light from each star since they both have the same point spread function. In STB the same BSA image and apertures are used to simultaneously measure both astrometry and net flux parameters. It is important to use the speckle analysis tools and parameters within STB in a consistent way, especially for photometry-related measurements, to keep from introducing small but unnecessary differences among the observations.

Since the BSA reconstructed image approaches zero wavefront error, it contains approximately the correct flux for each component star; this is the only photometric product. Flux Proportion (FP) is defined in equation (1), where A and B indicate the primary and secondary stars, respectively. Either net ADU or photoelectron signals give the same results. The sum of the A and B proportions is always 100%.

$$FP_A = ADU_A / (ADU_A + ADU_B)$$
$$FP_B = ADU_B / (ADU_A + ADU_B) \quad (1)$$

Flux Proportions for the four stars observed are presented in Figure 5. These plots were the first indication of both within-night and night-to-night BSA photometric repeatability. Each plot represents a within-night example

of repeatability, since multiple sets (3 to 6) of all four filters were observed in sequence. Night-to-night repeatability examples are provided by KR60AB (3 nights), and STF554 (2 nights).

For KR60AB (top row of Figure 5) the flux proportion trends are consistent, with remarkably small scatter (a few percent) for the B component, which at V~11.4 was the faintest star observed. However, there are significant shifts in the levels of the A and B proportions from night to night. Since there is good repeatability of the sets within each night, these shifts may be caused by night-to-night variation of atmospheric extinction. The differences could also represent intrinsic variability of one of the components; after the observations were made, KR60AB was found to be the flare star DO Cep (see Section 7.5).

Photometry was affected by the observatory's location at moderate elevation about 20 miles from the Pacific Ocean, where the "marine layer" frequently spoiled clear evenings with rising humidity, variable extinction, and transient clouds. FIRO was later relocated to a much better photometric site in Arizona.
STF554 (the very bright star 80 Tauri, bottom right of Figure 5) was observed on two nights of different photometric quality. The night of 1/15/2021 was degraded by high extinction, perhaps causing the odd wavelength distribution. The night of 2/6/2021 had the opposite weather pattern: high pressure, dry air, and no marine influence - a "photometric" night. The scatter is less, the secondary star is brighter, and the odd recurved trend with WL is absent. When the binary is dimmed by high extinction, the secondary star seems to suffer most, probably because its S/N declines significantly. Although the primary star has higher S/N, the sum of flux proportions for the components is always 1.0, so the primary star reflects the secondary scatter.

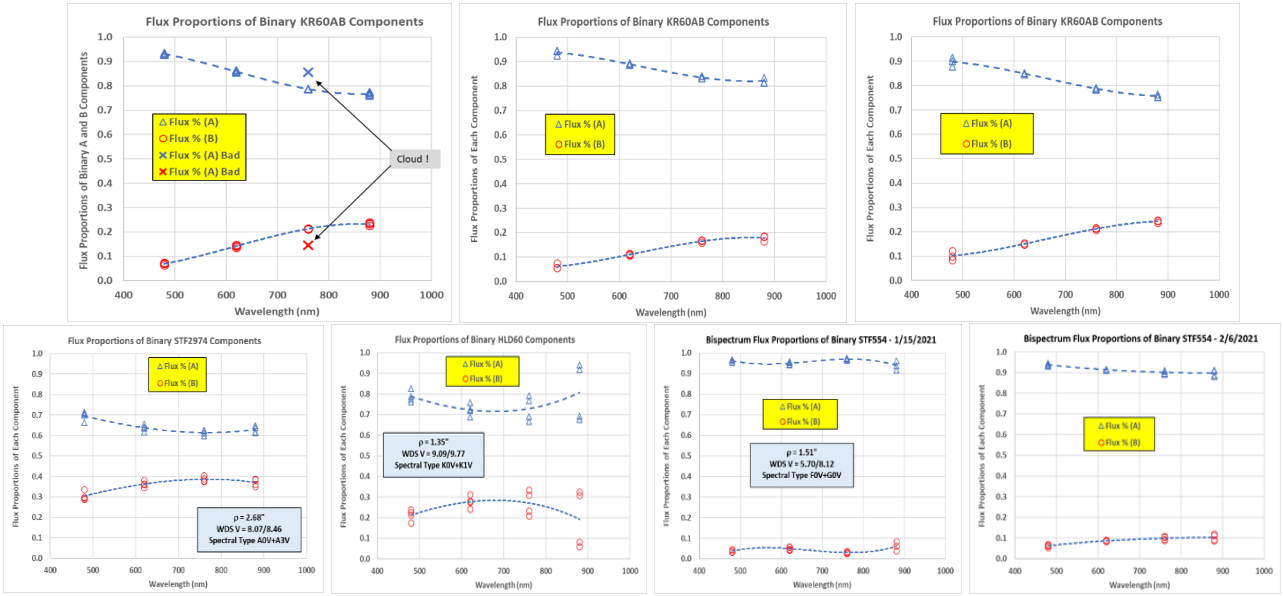

Figure 5. Flux Proportions measured for the A and B components of the 4 binary stars observed, plotted versus the center wavelength of each Sloan filter (Figure 2). Top row: KR60AB was observed in 2020 on 3 nights: 20 Oct (left), 31 Oct (middle) and 4 Dec (right). Repeatability is good, except for a cloud-affected image (X symbol) on the first night, ignored in further analysis. Bottom row: Left to right, flux proportions measured for the A and B components of STF2974 (5 sets), HLD60 (4 sets), and STF554 observed on two dates (5 sets on 1/15/2021, 4 sets on 2/6/2021).

The flux proportions for the binary HLD60 show large scatter because of variable extinction. Rapidly increasing marine layer extinction during the last two sets caused extremely low flux proportions for the B star (and correspondingly high for A), especially in the z′ filter. In further processing, the z′ data from those two sets was neglected. Several other binaries were observed, but only on nights so poor as to produce unusable photometric results.
Three conclusions can be drawn from the flux proportions of Figure 5:

(1) BSA flux proportion from STB is highly repeatable within a night, (less than a few percent at 11th magnitude).
(2) A photometric night is required for minimal photometric scatter.
(3) High extinction seems to affect the secondary (redder) star, probably by degrading its S/N more than the primary.

7.3 Long Exposures

Deep CCD exposures of the binary itself, taken in all-sky surveys such as SDSS, Pan-STARRS, and APASS, provide standard Sloan photometric magnitudes of the unresolved binary star. During long exposures in the speckle photometry method, the atmosphere mixes the close binary components into an unresolved seeing disk, just as it does in the survey images. In this way, the long exposures provide a means of self-calibration, without the need to observe a separate comparison star.

After speckle exposures for one filter are completed, the binary is immediately observed with 10 long exposures (typically each several seconds), much longer than the speckle exposures, but using the same filter and camera ROI. Taking the long exposures as near in time as possible to the speckle frames within each filter minimizes the time for significant atmospheric variations to develop, especially variable extinction. An example of a speckle BSA and a long exposure, taken back-to-back is shown in Figure 6.

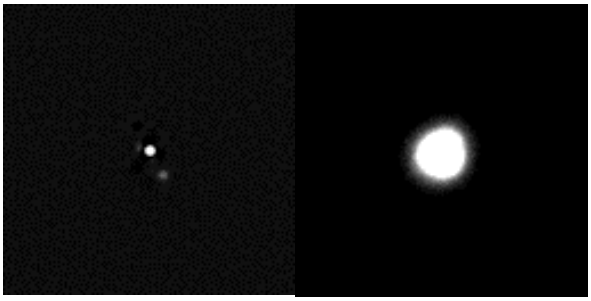

Figure 6. Examples of a diffraction limited BSA image reconstructed from 1000 speckle (60 msec) frames (left) and a stack of 5 long (10 sec) unresolved exposures taken immediately following (right). The images are binary KR60AB, r′ filter, 128x128 pixels, 22"x22" in size.

The approach of taking long exposures is a variation on the common practice of differential photometry of variable stars, but without the wider field needed to include comparison and check stars in CCD imaging. The long exposures of the target binary itself play the role of a "secondary standard" comparison star, providing a way to transform the instrumental magnitude to the standard photometric system.

The long images are stacked to produce a single image with high S/N and a more symmetric psf. Binaries having $\rho > 3$" were not considered, because the atmosphere may not blend the components well enough, and because wider components are unlikely to be in the same speckle isoplanatic patch.

The flux is measured in STB with a photometric aperture suitable for the seeing disk, much larger than for the two stars in the BSA image. The same aperture - large enough to include all the light in all four bands - is desirable for consistency of color index calibration. At longer wavelengths, the opposite effects of larger psf and reduced atmospheric blurring (better seeing) tend to offset each other. Wide separation may lead to asymmetric star images, but a larger photometric aperture can still include all the light, albeit with added background noise.

A fundamental assumption is that neither component of the binary is a variable star because that would affect the archived survey magnitudes used in calibration, and the resulting spectral types. However, small-amplitude variability is common and constitutes an added noise source. If one component were a variable star with large

amplitude (i.e., well above the noise of the photometry), its approximate light curve might be measurable over a series of observations.

It may be possible to eliminate the long calibration exposures by processing the speckle exposures in a different way, by, in addition to BSA, stacking all the short speckle exposures to create a single long exposure with an equivalent unresolved atmospheric seeing disk. This would save observation time but would require care in centroiding to account for telescope tracking drift. This technique could be explored in the future.

7.4 Photometric Self-Calibration

The only steps in processing the long exposure images are stacking them to create a single high S/N image for each filter, and then measuring the net flux in STB. For consistency of color index calibration, the same size aperture is used for all four filters, and the net ADU flux within the aperture is converted to photoelectrons per second to account for camera gain and different exposure times for different filters. The instrumental magnitude of the unresolved binary is then calculated with equation (2).

$$m_{(A+B)} = -2.5 * \text{Log}_{10}(\text{Net Flux}_{A+B}) \qquad (2)$$

For each filter, the instrumental magnitude (m) is then compared with the standard magnitude (M) from survey catalogs. The AAVSO APASS photometric survey catalog, Data Release 10 (AAVSO, 2020), has generally been used because it has brighter magnitude limits, includes magnitudes for all four Sloan filters more consistently, and is more easily accessed than other large photometric surveys. A Calibration Factor, simply a magnitude difference, is calculated per equation (3).

$$Z_{A+B} = (M_{\text{Standard}} - m_{\text{Instrumental}})_{A+B} \qquad (3)$$

This calibration factor includes instrumental transformation to the standard system, so it is valid for only one filter at a time. It also includes the variable atmospheric extinction terms which impact photometry: air mass, sky transparency, and extinction effect on color. A new series of long exposures is observed to "re-calibrate" every series of speckle frames, since sky conditions may vary rapidly. The calibration factors, $Z_{g'}$ $Z_{r'}$ $Z_{i'}$ $Z_{z'}$ for the g' r' i' z' filters within a set, are the final product of each set of long exposures, shown in Figure 7.

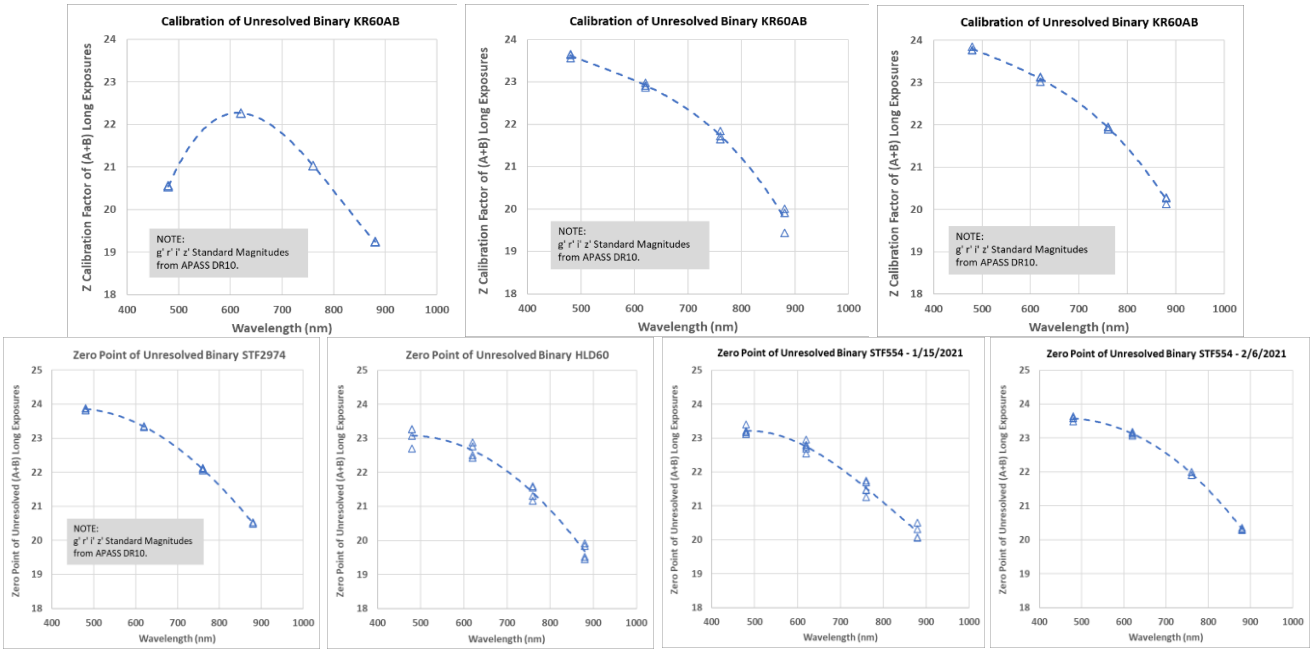

Figure 7. Calibration Factors ("Zero Points") measured for the unresolved long exposures of the 4 binary stars observed, plotted versus the center wavelength of each Sloan filter (Figure 2). Z is the magnitude difference from equation (3). Top row: KR60AB observed on 3 nights in 2020: 20 Oct (left), 31 Oct (middle) and 4 Dec (right). The KR60AB calibration factors have good repeatability. Bottom row, Left to right: the calibration factors measured for STF2974 (5 sets), HLD60 (4 sets), and STF554 observed on two dates (5 sets on 1/15/2021, 4 sets on 2/6/2021). High scatter again betrays the HLD60 and STF554 (1/15/2021) results as suffering variable extinction. Good repeatability of the STF2974 and later STF554 (2/6/2021) calibrations indicate steady extinction.

The long exposures are the only photometric calibration used in this method, i.e., they *define* the calibration factors which transform the unresolved star instrumental magnitude to the standard Sloan system. In some ways the calibration factors are analogous to the zero points of all-sky photometry; however, they are only a short-cut global approximation of all combined photometric correction terms, not a rigorous determination of extinction corrections and instrumental transformation based on measurements of standard stars. In effect, the binary star itself is treated as a secondary standard star for self-calibration. This approach is something like differential photometry, where the long exposures play the role of a "comparison star" to adjust an instrumental magnitude to a standard system magnitude. In the spirit of differential photometry, a better technique might take long exposures both *before and after* the speckle frames, then use the average to get the calibration factor, overlapping the time and conditions of the speckle frames better.

Several sets (3 to 6) were observed each night, and all the sets are included in Figure 7. Large variations from night to night, or smaller "scatter" from set to set within a night, generally indicate that atmospheric extinction was variable (transparency and/or airmass). Good calibration repeatability (within the size of the plotted symbols) indicates steady extinction: a "photometric" night. The calibration factors serve both to adjust the photometry to the standard Sloan system, and to account for atmospheric variations, enabling correction of the speckle BSA flux proportions to Sloan magnitudes, even in the presence of moderately changing conditions.

A key assumption is that the calibration factor, measured from the unresolved *combined* light of both components, can be applied to the *individual* A and B stellar components. This assumption seems reasonable for similar stellar types and colors, but might cause systematic errors in the B star for high delta magnitude binaries, where the primary star dominates the long exposures, but A and B have much different colors or S/N.

In our development of the speckle photometry method, standard photometric image calibration using bias, dark, and flat frames was not done; therefore, some noise is present which might be suppressed by careful calibration. However, lack of calibration is mitigated by the following factors: (1) the speckle and "long" calibration frames are short (only a few seconds), (2) the cooled camera has very low dark current (<1e^-/sec), (3) CMOS cameras now have very low read noise (~1e^-), remarkably uniform "bias" levels and no "amp glow," (4) the highly magnified image is spread across many pixels (typically 6-8 pixels across the Airy disk) rather than only a few pixels as in wide-field photometry, (5) pixel variations are further averaged by random signal sampling across many pixels within the ROI due to atmospheric scattering and small tracking errors during many speckle frames and multiple "long" exposures. Additionally, it is very difficult to be certain that the small ROI used in data frames is correctly registered in full size calibration frames. Therefore, shot noise during short speckle exposures, especially for faint secondary components, is likely the dominant noise source.

7.5 Component Standard Magnitudes

The instrumental fluxes of the binary A and B components are calculated from equation (4), where the combined instrumental flux measured from the stacked long exposures (equation 2) is simply multiplied by the respective flux proportion of each component (equation 1) measured from the reconstructed BSA image.

$$\text{Net Flux}_A = \text{Net Flux}_{A+B} * FP_A$$
$$\text{Net Flux}_B = \text{Net Flux}_{A+B} * FP_B \qquad (4)$$

The instrumental magnitude of each component is then calculated from equation (5).

$$m_A = -2.5 * \text{Log}_{10}(\text{Net Flux}_A)$$
$$m_B = -2.5 * \text{Log}_{10}(\text{Net Flux}_B) \qquad (5)$$

Finally, standard magnitudes of the components are estimated simply by adding the calibration factor back to their instrumental magnitudes, equation (6). This key assumption of the method bears restating: although the calibration factor is *derived from the unresolved star*, it is *applied to each component* of the binary separately, to estimate its standard magnitude.

$$M_{A\ \text{Standard}} = m_{A\ \text{Instrumental}} + Z_{A+B}$$
$$M_{B\ \text{Standard}} = m_{B\ \text{Instrumental}} + Z_{A+B} \qquad (6)$$

The resulting estimated standard magnitudes of the four binary stars observed are shown in Figure 8. Standard Sloan magnitudes of the KR60AB components are shown in the top row for the three nights observed. The A star is reasonably constant and consistent with the APASS10 survey, but the B star is significantly fainter. WDS magnitudes (Johnson V) are 9.93/11.41, or Δmag ~1.5, but at the V filter center WL (~540nm) the estimated Δmag is ~2.4 in Figure 8, almost a full magnitude fainter. Additionally, the B star varies by about 0.5 magnitude over the 3 nights. After the observations were made it was found that K60AB is the known flare star DO Cep, but it is not certain which component is the source of the flares.

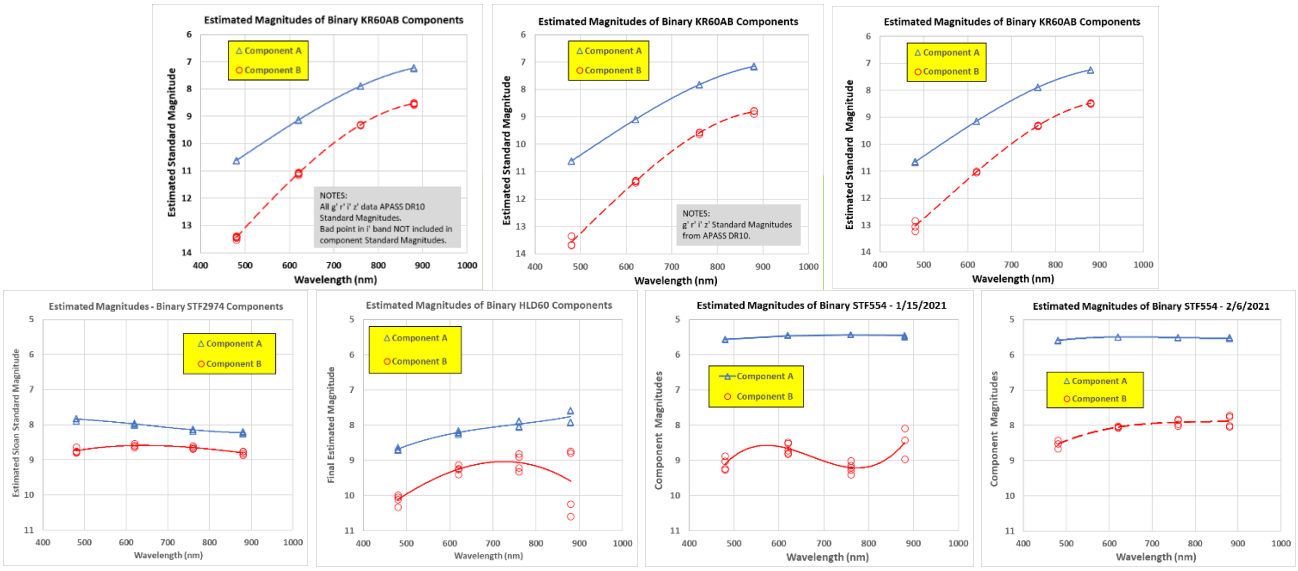

Figure 8. Estimated standard g' r' i' z' magnitudes of the A (blue) and B (red) components, based on the flux proportions of Figure 5 and the calibration factors of Figure 7.Top row: Standard Sloan magnitudes for KR60AB on 20 Oct 2020 (left), 31 Oct 2020 (middle) and 4 Dec 2020 (right). Both components have high slopes because they are cool, red, late type (M) dwarf stars. Bottom row, left to right: standard magnitudes for the A and B components of STF2974 (5 sets), HLD60 (4 sets), and STF554 observed on two dates (5 sets on 1/15/2021, 4 sets on 2/6/2021).

The B star variations could also be caused by variable 2nd-order (color) extinction, which is not well accounted for by the calibration factor when the two stars have significantly different colors, as discussed further in Section 7.6. Lower S/N for the B star also contributes, indicated by more scatter within a night, especially for the g' and z' filters, where the star is faint or the QE is low, respectively. The odd wavy character of the secondary star STF55B on 1/15/2021 reflects that of the flux proportions of in Figure 5, probably caused by high or variable extinction. Table 3 provides all the observed Sloan standard magnitudes, together with uncertainties derived from the repeated sets of observations each night. The data for STS554B on that 1/15/2021 are highlighted in orange, indicating poor quality.

APASS10 standard magnitudes of the unresolved binary are generally used as the "truth model" for long exposure calibration. However, APASS10 data were not available for the bright binaries HLD60 and STF554. GaiaDR2 resolved these binaries and provided G Bp Rp photometry data for both components. Therefore, the combined magnitudes of the A and B components from the ATLAS Catalog were used for calibration. The ATLAS All-Sky Stellar Reference Catalog (Tonry et al. 2018) and (Carrasco 2015) is a major product of Gaia DR2, containing photometric data transformed to other major photometric systems including the PanSTARRS version of the Sloan g' r' i' z' bands.

Table 3. Summary of Sloan standard magnitude measurements. The orange-highlighted data are not reliable because of high or variable extinction.

KR60AB - 10/20/2020								
Component	Sloan Standard Magnitudes							
	g'	σ g'	r'	σ r'	i'	σ i'	z'	σ z'
A	10.620	0.004	9.134	0.006	7.891	0.003	7.231	0.010
B	13.437	0.058	11.088	0.037	9.309	0.009	8.532	0.032

KR60AB - 10/31/2020								
Component	Sloan Standard Magnitudes							
	g'	σ g'	r'	σ r'	i'	σ i'	z'	σ z'
A	10.612	0.013	9.095	0.004	7.827	0.007	7.159	0.014
B	13.570	0.188	11.361	0.036	9.587	0.034	8.817	0.066

KR60AB - 12/4/2020								
Component	Sloan Standard Magnitudes							
	g'	σ g'	r'	σ r'	i'	σ i'	z'	σ z'
A	10.659	0.023	9.145	0.004	7.890	0.005	7.247	0.007
B	13.034	0.196	11.026	0.021	9.313	0.020	8.483	0.023

STF2974 11/28/2020								
Component	Sloan Standard Magnitudes							
	g'	σ g'	r'	σ r'	i'	σ i'	z'	σ z'
A	7.851	0.033	7.977	0.021	8.154	0.022	8.224	0.028
B	8.719	0.072	8.592	0.037	8.637	0.035	8.805	0.048

HLD60 - 12/15/2020								
Component	Sloan Standard Magnitudes							
	g'	σ g'	r'	σ r'	i'	σ i'	z'	σ z'
A	8.681	0.038	8.208	0.043	7.970	0.090	7.923	0.018
B	10.114	0.151	9.253	0.113	9.062	0.244	8.763	0.038

STF554 - 1/15/2021								
Component	Sloan Standard Magnitudes							
	g'	σ g'	r'	σ r'	i'	σ i'	z'	σ z'
A	5.566	0.007	5.450	0.008	5.433	0.005	5.474	0.027
B	9.100	0.183	8.663	0.157	9.204	0.146	8.496	0.443

STF554 - 2/6/2021								
Component	Sloan Standard Magnitudes							
	g'	σ g'	r'	σ r'	i'	σ i'	z'	σ z'
A	5.595	0.001	5.493	0.001	5.512	0.002	5.523	0.003
B	8.534	0.012	8.054	0.003	7.914	0.012	7.881	0.021

7.6 Component Color Indices

Color index is the difference in magnitude between any two filters. Measuring color indices of the A and B components of a binary star on the standard Sloan photometric system is a major goal of this speckle photometry method. Therefore, the four filters are observed together in a set, combining short speckle and long calibration exposures, close together in time as described in Section 6.

Six color indices are formed from the four g' r' i' z' filters: (g'-r'), (g'-i'), (g'-z'), (r'-i'), (r'-z'), and (i'-z'). Color indices are taken only from measurements within the same set. All six color indices are equally valid, but an error in any one standard magnitude will propagate into three of the color indices. Each set provides an independent sample of all six color indices and the overall average and statistics are derived from all the sets in a nightly observation.

Most photometric correction terms will tend to cancel in this method, as they do in differential photometry, where the variable and comparison stars are observed under nearly the same conditions.

However, the 2nd-order extinction term, which corrects for color, does not cancel for stars of significantly different colors. It is not well accounted for in this method because it includes the color index times airmass; color index is large for red stars, and airmass is never less than 1. This is analogous to using a comparison star of much different color in differential photometry. Therefore, 2nd-order extinction may add a systematic error to the magnitudes and color indices of a blue-red binary, particularly to the redder star.

Color Index results are compared in Figure 9, plotted in order of the "normalized wavelength" parameter (ΔWL / Average WL) that accounts for both WL difference and the region in which the difference occurs. The normalized WL places the color indices in order of increasing sensitivity to star color. This trend should be monotonic, although we are aware of no reason why it must be strictly linear; nevertheless, the data are shown with a linear regression fit simply for reference. Points for the primary (brighter) stars are generally closer to their blue line, while the scatter is generally more severe about the red line for the secondary (fainter) stars, indicating that much of the scatter may be caused by lower S/N.

In the case of KR60AB - two red dwarf stars - some of the scatter may be artifacts of photometric transformation for red stars; however, underlying astrophysical characteristics could also arise from molecular absorption bands that begin to appear in cool red stars. The highly scattered indices for STF554B on 1/15/2021 are suspect, producing a slope almost the same as the much earlier primary star. On 2/6/2021, the better sky produced less scatter and a more reasonable result.

Figure 9 suggests a general pattern: the linear regression slope seems to increase with star spectral type (discussed further in Section 7.7). These characteristics, arranged from early toward later types are:
STF2974 (A0V+A3V) negative/small slope
STF554 (F0V+G2V) small positive slope
HLD60 (K0V+K1V) moderate positive slope
KR60AB (M3.5V+M4.5V) large positive slope

Internal uncertainties of color index measurements for the A and B component stars are estimated in Figure 10. These uncertainties are the standard deviations relative to the linear fits of Figure 9. It is clear that the uncertainties of the secondary components are significantly greater than the primary, probably caused by lower S/N and variable extinction.

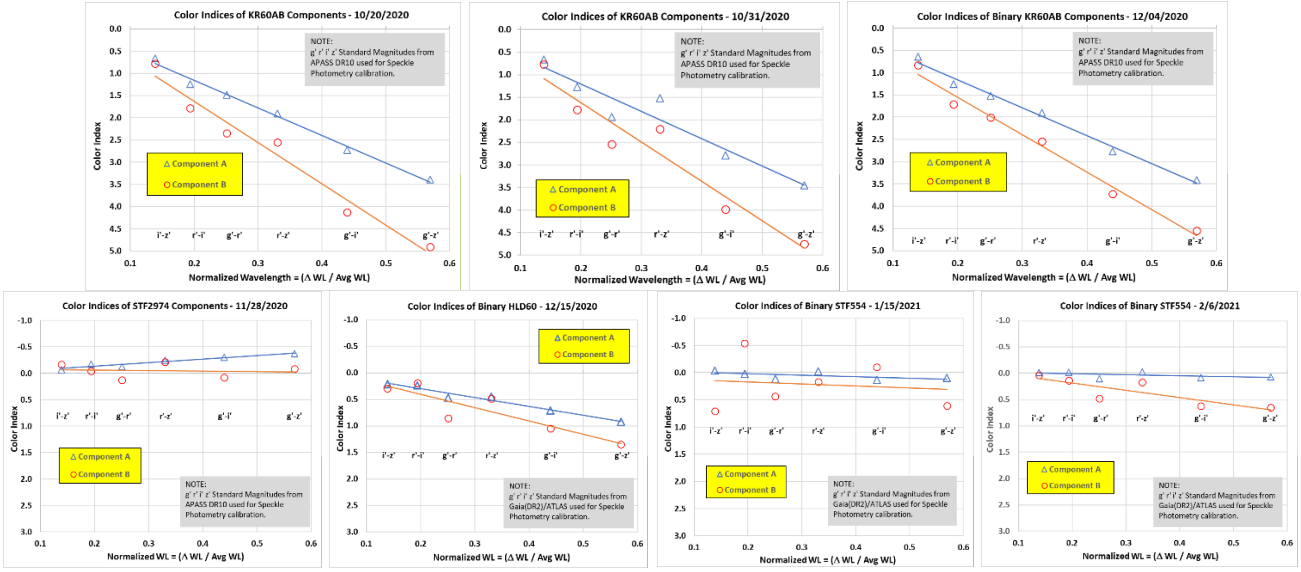

Figure 9. Color indices measured for each of the 7 observations, plotted against normalized WL. Each point is the average of all sets observed for that star, noted with date in the heading of each plot. The filters composing each color index are given below the plotted points.

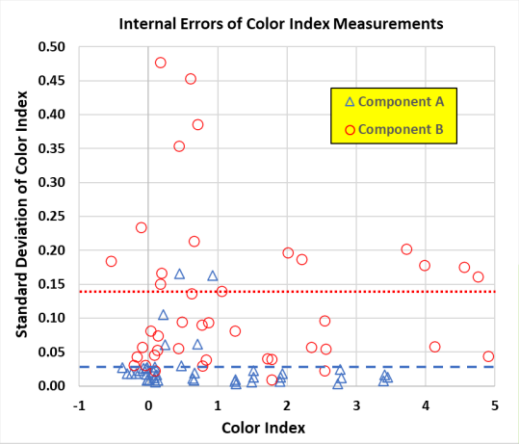

Figure 10. Standard deviations of the Color Indices derived from all sets of measurements taken on each night. The range of measured color indices (horizontal axis) arises from the 6 Sloan filter combinations applied to 8 stars having a range of colors. RMS uncertainties are: primary star 0.029 magnitude (blue dashed line), secondary star 0.138 (red dotted line).

The four extremely high points in Figure 10 all occurred for the B component of STF554 (~3 magnitudes fainter than A) on the night of 1/15/2021, already noted in Figures 5 and 7 as having variable extinction. The overall RMS of these color index errors is 0.029 magnitude for the primary star and 0.138 for the secondary star, roughly comparable with uncertainties estimated by Horch et al. (2001 & 2004) for small telescopes (~0.15).

7.7 Component Spectral Types

The foundation of spectrophotometry was laid by correlating Johnson U B V photometry color indices with Morgan-Keenan spectroscopic standard stars (Johnson & Morgan, 1953). As detectors became more red-sensitive, the correlation was extended to the Johnson-Kron-Cousins U B V Rc Ic bands. These J-C color index relationships to spectral type were refined to a continuous set by Pecaut & Mamajek (2013), then further refined, expanded, and made accessible on the web site of Mamajek (2019), which was the source for this work. The Mamajek tables are limited to normal dwarf stars on the main sequence that are near enough to the Sun not to be significantly reddened by interstellar dust.

A photometric transformation was required from Johnson-Cousins B V Rc Ic magnitudes in the Mamajek tables to the Sloan g' r' i' z' system. The transformation set of Rogers, et al. (2006) was used, Table 4. The resulting spectrophotometric tables of Mamajek, transformed to Sloan color indices, are plotted in Figure 11. Each of the six color indices has a unique and equally valid relationship with spectral type. The color index correlations are continuous and monotonically increase with spectral type.

The spectral types are uniformly divided into a sequence of sub-types from B0 through M9. The Mamajek tables provide a Sloan color index value for each spectral sub-type and a corresponding integer spectral parameter shown on the bottom axis of Figure 11.
Table 4. The equations transforming Johnson-Cousins B V Rc Ic photometry bands to Sloan g' r' i' z' bands.

Rogers et al (2005) Transformations from J-C to Sloan for Main Sequence Stars, Unreddened
$g' = V - 0.042*(B-V)^2 + 0.602*(B-V) - 0.087$
$g'-r' = 0.278*(B-V) + 1.321*(V-Rc) - 0.219$
$r'-i' = 1.000*(Rc-Ic) - 0.212$
$r'-z' = 1.567*(Rc-Ic) - 0.365$

For an observed color index, the value of that parameter is linearly interpolated, corresponding to a spectral sub-type with an added decimal point. Referring to Figure 11 for example, if a measured g'-i' color index is 1.05, the interpolated parameter value is 43.1, or spectral type K3.1V. In this way, each measured color index directly provides an estimate of spectral type.

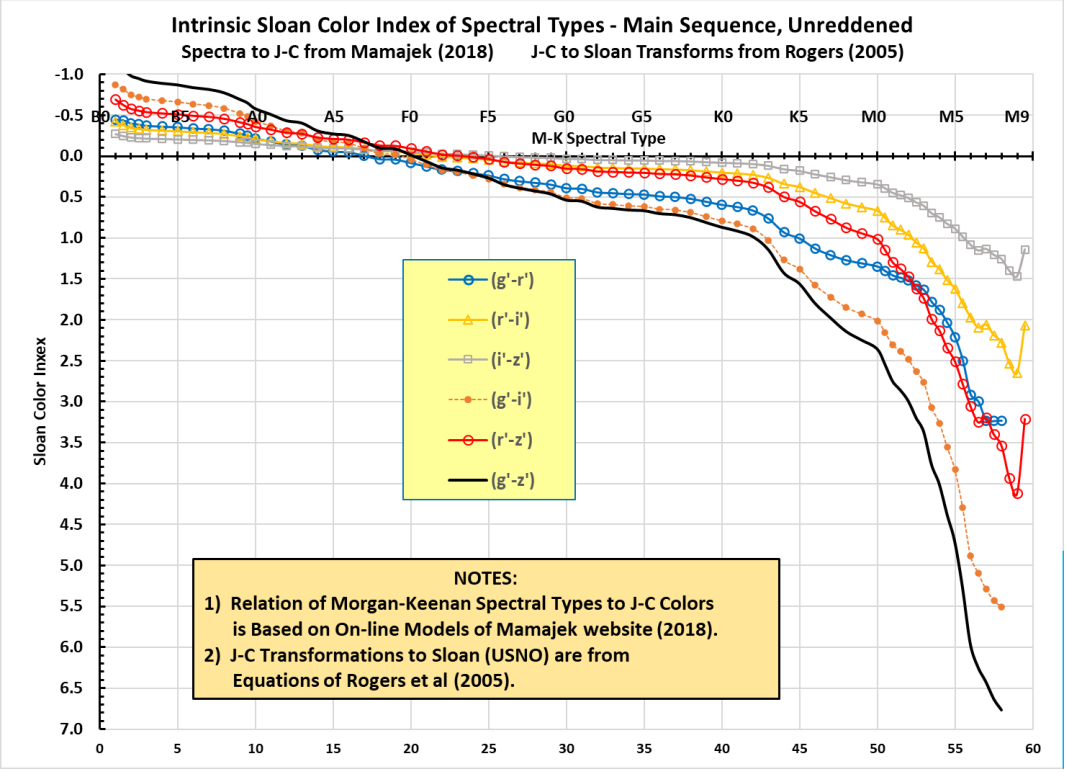

Figure 11. The relationship of Sloan filter color indices to spectral type for main sequence dwarf stars, based on the tables of Mamajek, with transformation from J-C to Sloan. Spectral type is indicated at top and the integers at bottom correspond to integers of spectral sub-type (e.g., 30=G0, 31=G1, 32=G2, ...). This parameter is used to interpolate spectral type from measured color index.

The components of the four initially observed binary stars sample a broad range of spectral types: A F G K M. To estimate overall spectral type of each star from the six observed color indices, three methods of correlation were explored: average, weighted average, and slope. The average method is simply the average of the integer parameters of all six color indices.

In the weighted average method, each parameter is scaled by its color index sensitivity (normalized wavelength in Figure 9) before taking the average. Therefore, the color indices of more widely separated filters are given greater weight.

In the slope method, the same linear regression approach shown in Figure 9 was applied to the Mamajek color indices for the whole range of spectral types, forming the monotonic family of slopes seen in Figure 12 as the solid black curve. Of course, this locus of slopes has a similar character to the indices in Figure 11. The slopes of the observed binaries are also plotted at their interpolated integer spectral parameter; therefore, each measured slope falls on the black line at its estimated spectral type. The WDS points (small solid symbols) were added to Figure 12 as references for the observed points, and the displacement along the curve from the measured point to the WDS point indicates their level of agreement. There are two points for each STF554 component, and three for KR60, corresponding to the number of nights observed.

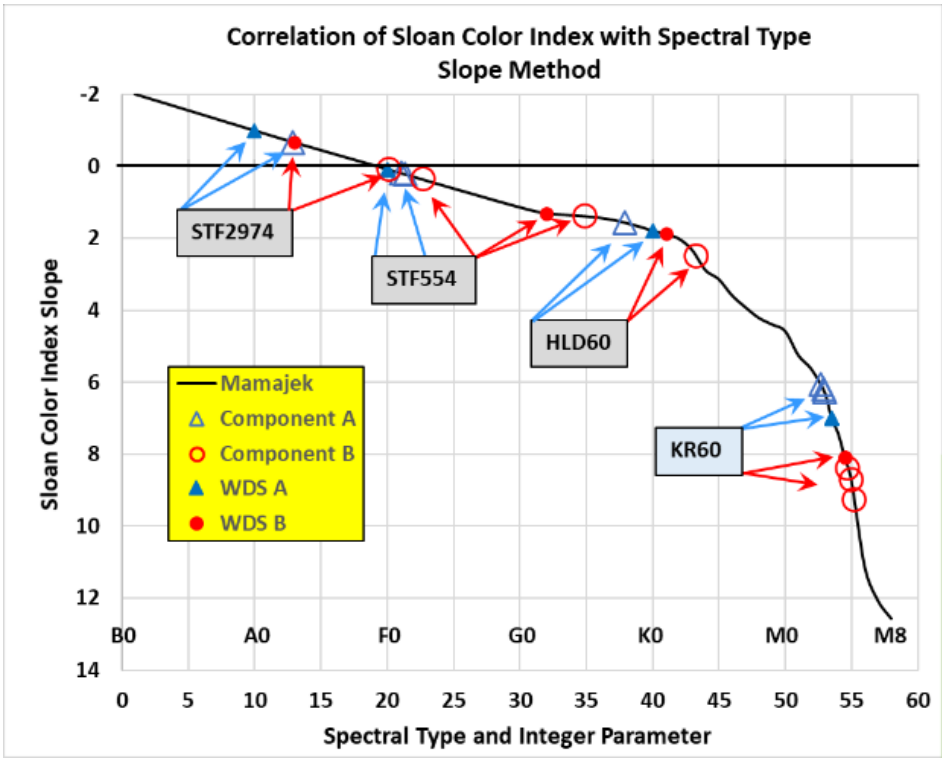

Figure 12. When the Sloan color indices from the Mamajek tables (Figure 11) are plotted against the normalized WL (Figure 9), their slopes form a monotonic family of points, the black curve. WDS (solid symbols) and slope method results (open symbols) are also shown.

It is noted in Figure 12 that the two observed dates for STF554 give much different spectral types for the B star. This was caused by the large color index scatter on the night of 1/15/2021, already noted from Figures 9 and 10, indicating that the slope method may be overly sensitive to errors in color index. The G5V estimate by the slope method on 2/6/2021 is probably more correct because the atmosphere was quite stable that night.

Results of all measured color indices are presented in Table 5, and the three spectral correlation methods are compared with the WDS spectral types, verified in Simbad. They are not exact matches, but the estimated spectral types are remarkably self-consistent, and agree reasonably well with WDS. The average and slope methods are often identical. The slope method may offer further astrophysical insight, but that is not explored here. There is no obvious "best" correlation method, but the simple average method may be less sensitive to errors in color index, and it will probably be the method of choice going forward.
Table 5 also shows the spectral type of STF554B as G2V, which is a Simbad update to G0V in WDS. On the night of 1/15/2021, the erratic color index (r'-i') = -0.542 (orange highlight) was beyond the range of the Mamajek tables, so it provided no interpolated parameter. The large scatter that night also affected the slope

method greatly (also orange), shifting the estimated spectral type by almost a whole letter type. The results of 2/6/2021 are more reliable because the extinction was lower and steady.

Table 5. Color Indices and comparison of estimated Spectral Type results for the three correlation methods. Columns, left to right: binary star component, six measured Sloan color indices, resulting interpolation parameter from the three methods, estimated spectral type from each method, and WDS spectral type.

KR60AB - 10/20/2020													
Component	Average Color Indices						Interpolation Parameter			Spectral Type			
	i'-z'	r'-i'	g'-r'	r'-z'	g'-i'	g'-z'	Average	Wt Avg	Slope	Average	Wt Avg	Slope	WDS
A	0.660	1.243	1.486	1.903	2.729	3.389	52.9	52.8	52.9	M2.9V	M2.8V	M2.9V	M3.5V
B	0.777	1.780	2.349	2.556	4.128	4.905	55.1	55.2	55.2	M5.1V	M5.2V	M5.2V	M4.5V
KR60AB - 10/31/2020													
Component	Average Color Indices						Interpolation Parameter			Spectral Type			
	i'-z'	r'-i'	g'-r'	r'-z'	g'-i'	g'-z'	Average	Wt Avg	Slope	Average	Wt Avg	Slope	WDS
A	0.668	1.268	1.517	1.936	2.785	3.453	53.0	53.0	52.7	M3.0V	M3.0V	M2.7V	M3.5V
B	0.770	1.774	2.209	2.544	3.983	4.753	55.0	55.1	55.0	M5.0V	M5.1V	M5.0V	M4.5V
KR60AB - 12/4/2020													
Component	Average Color Indices						Interpolation Parameter			Spectral Type			
	i'-z'	r'-i'	g'-r'	r'-z'	g'-i'	g'-z'	Average	Wt Avg	Slope	Average	Wt Avg	Slope	WDS
A	0.644	1.254	1.514	1.898	2.768	3.412	53.0	52.9	53.0	M3.0V	M2.9V	M3.0V	M3.5V
B	0.830	1.714	2.008	2.544	3.721	4.551	54.8	54.8	54.8	M4.8V	M4.8V	M4.8V	M4.5V
STF2974 11/28/2020													
Component	Average Color Indices						Interpolation Parameter			Spectral Type			
	i'-z'	r'-i'	g'-r'	r'-z'	g'-i'	g'-z'	Average	Wt Avg	Slope	Average	Wt Avg	Slope	WDS
A	-0.070	-0.176	-0.126	-0.246	-0.303	-0.373	13.6	13.1	12.9	A3.6V	A3.1V	A2.9V	A0V
B	-0.168	-0.045	0.127	-0.213	0.082	-0.086	17.4	18.8	20.2	A7.4V	A8.8V	F0.2V	A3V
HLD60 - 12/15/2020													
Component	Average Color Indices						Interpolation Parameter			Spectral Type			
	i'-z'	r'-i'	g'-r'	r'-z'	g'-i'	g'-z'	Average	Wt Avg	Slope	Average	Wt Avg	Slope	WDS
A	0.047	0.239	0.472	0.286	0.711	0.758	37.9	38.1	37.9	G7.9V	G8.1V	G7.9V	K0V
B	0.299	0.191	0.861	0.490	1.052	1.351	43.7	43.4	43.3	K3.7V	K3.4V	K3.3V	K1V
STF554 - 1/15/2021													
Component	Average Color Indices						Interpolation Parameter			Spectral Type			
	i'-z'	r'-i'	g'-r'	r'-z'	g'-i'	g'-z'	Average	Wt Avg	Slope	Average	Wt Avg	Slope	WDS
A	-0.041	0.018	0.116	-0.023	0.133	0.093	21.6	21.5	21.3	F1.6V	F1.5V	F1.3V	F0V
B	0.709	-0.542	0.437	0.167	-0.105	0.604	33.1	31.5	22.8	G3.1V	G1.5V	F2.8V	G2V
STF554 - 2/6/2021													
Component	Average Color Indices						Interpolation Parameter			Spectral Type			
	i'-z'	r'-i'	g'-r'	r'-z'	g'-i'	g'-z'	Average	Wt Avg	Slope	Average	Wt Avg	Slope	WDS
A	-0.011	-0.019	0.102	-0.030	0.082	0.072	21.6	21.1	21.0	F1.6V	F1.1V	F1.0V	F0V
B	0.034	0.139	0.481	0.173	0.620	0.654	33.1	33.8	35.0	G3.1V	G3.8V	G5.0V	G2V

8. Summary of Key Assumptions

The speckle photometry method relies on six key assumptions:

- Speckle bispectrum analysis produces the correct flux proportions for binary star components.
- The simple global calibration factor, derived from photometry of the unresolved binary in long exposures, fully transforms instrumental magnitudes to standard Sloan magnitudes.
- The calibration factor, derived from the combined light of both components, is also valid for the A and B binary components individually, but may introduce systematic errors from color difference in early-late binary components.

- Photometry of large surveys provide secondary standard star magnitudes accurate enough to estimate spectral types.
- Variability of one or both components would impact the standard magnitude and color index correlations. However, large variability of one component may be detectable over a series of observations.
- The correlations of spectral type with Johnson-Cousins color indices in the Mamajek tables are still valid when transformed to the Sloan photometric system.

9. Conclusions

Although this was only the first exploration of the speckle photometry method, we were able to draw a number of tentative conclusions:

- Speckle BSA processing in STB gives repeatable flux proportions.
- The primary sources of error are probably shot noise from low signal in some filters (i.e., the combination of filter, camera QE and star color), and high or rapidly varying extinction.
- The effects of extinction at different wavelengths (2^{nd}-order color terms) may cause significant photometric errors for binary components of different colors and/or high Δmagnitude but could not be evaluated from these initial observations.
- "Long" exposures of a few seconds give reasonable photometric calibration, using the binary star itself as a secondary photometric standard.
- Many of the binaries with known spectral type for both components are relatively bright, making it difficult to find g' r' i' z' magnitudes from photometric surveys. APASS10 has the most consistent Sloan data for brighter stars. Gaia ATLAS transformations (not discussed here) may also be used.
- Color indices were measured accurately enough to make reasonable estimates of component spectral types, especially under good atmospheric conditions. Non-photometric nights produced unusable results and are to be avoided.
- Photometric nights provided good results with small scatter, but marginal nights (high humidity or high extinction) produced more scatter, even when employing frequent calibration exposures.
- Estimated component spectral types are remarkably self-consistent and agree reasonably well with WDS Catalog types.
- The three methods explored for estimating spectral type gave very consistent results, except when there was large photometric scatter. The average method will probably be used in further observations.
- The speckle photometry method provided reasonable estimates of component spectral types, for the range of A F G K M normal dwarf stars observed.
- A change in the sequence of observation may reduce photometric scatter, by observing half (~5) of the long exposures before the speckle exposures, and then the other half after the speckle frames.
- Processing the speckle exposures by stacking may make it possible to build a single equivalent calibration image with an unresolved atmospheric seeing disk. This technique could eliminate the separate long calibration exposures and may be explored in the future.
- Further observations of close binaries are planned to refine and validate the method.
- It is hoped that the speckle photometry method will provide complimentary information to improve the quality of stellar masses in binary orbit solutions and a more complete picture of stellar properties.

10. Acknowledgements

This research has made use of the Washington Double Star Catalog and 6^{th} Orbit Catalog, maintained at the U.S. Naval Observatory; the AAVSO Photometric All-Sky Survey (APASS) funded by the Robert Martin Ayers Sciences Fund and NSF AST-1412587; the SIMBAD, VizieR and Aladin features of the Strasbourg Astronomical Data Center (CDS); and results from the European Space Agency's Gaia mission. Gaia DR2 data was processed by the Gaia Data Processing and Analysis Consortium (DPAC), funded by national institutions participating in the Gaia Multi-Lateral Agreement (MLA).

The authors very much appreciate the Sidereal Technology control system electronics and comprehensive SiTech ZWOCam user interface software enabling remote speckle observations, provided by Dan Gray.

11. References

Altunin, I., Wasson, R., Genet, R., "Observations of Potential Gaia DR2 Red Dwarf Binary Stars in the Solar Neighborhood – II," *JDSO*, **16-5**, 470, November 2020.

AAVSO web site, 2020. https://www.aavso.org/download-apass-data

Caputo, R., Marchetti, C., Teagarden, J., Armstrong, J.D., Wiese, C., Tock, K., Genet, R., Harshaw, R., Wasson, R., Freed, R., "First Remote Student Speckle Interferometry Double Star Observations on the InStAR Student Robotic Telescope Network," *JDSO*, **16-5**, 458, November 2020.

Carrasco, Joseph M., Gaia web site, Section 5.3.7 "Photometric relationships with other photometric systems," https://gea.esac.esa.int, taken from S. Alam, F. D. Albareti, C. Allende Prieto, F. Anders, S. F. Anderson, T. Anderton, B. H. Andrews, E. Armengaud, É. Aubourg, S. Bailey d et al., 2015. "The 11th and 12th Data Releases of the Sloan Digital Sky Survey: Final Data from SDSS-III." *ApJS*, **219**, pp. 12.

Davidson, James W. Jr., Brian J. Baptista, Elliott P. Horch, Otto Franz, and William F. van Altena, 2009. "A Photometric Analysis of Seventeen Binary Stars Using Speckle Imaging," *The Astronomical Journal*, **138,** pp 1354–1364, November 2009.

Gray, Dan, et al., 2020. Personal communications.

Harshaw, R., Rowe, D., Genet, R., 2017. "The Speckle Toolbox: A Powerful Data Reduction Tool for CCD Astrometry," *Journal of Double Star Observations*, **13-1**, 52, January 2017.

Horch, Elliott P., Zoran Ninkov, Otto G. Franz, 2001. "CCD Speckle Observations of Binary Stars from the Southern Hemisphere - III. Differential Photometry," *The Astronomical Journal*, **121**: 1583, March 2001.

Horch, Elliott P., Meyer, Reed D., van Altena, William F., 2004. "Speckle Observations of Binary Stars with the WIYN Telescope - IV. Differential Photometry," *The Astronomical Journal*, **127**, 1727–1735, March 2004.

Horch, Elliott P., 2006. "The Status of Speckle Imaging in Binary Star Research," *RevMexAA (Serie de Conferencias)*, **25**, 79–82, 2006.

Johnson, H.L. and Morgan W.W., 1953. "Fundamental Stellar Photometry for Standards of Spectral Type on the Revised System of the Yerkes Spectral Atlas," *Astrophysical Journal*, **117**, pp 313–352, 1953.

Mamajek, E.E., 2019. University of Rochester website of Eric Mamajek: http://www.pas.rochester.edu/~emamajek/EEM_dwarf_UBVIJHK_colors_Teff.txt, Version 2019.3.22.

Marchetti, Calla, Ryan Caputo, and Russell Genet, 2020. "The Fairborn Institute Robotic Observatory: First Observations," *JDSO*, **16-5**, 444, November 2020.

Marchetti, C., Duan, X. and Nordenholz, S., 2021. "Remote Speckle Interferometry of Undiscovered Double Stars," *JDSO*, **17-1**, 81, January 2021.

McAlister, Harold A., 1985. "High Angular Resolution Measurements of Stellar Properties," *Annual Review of Astronomy & Astrophysics*, **23**, 59-87, 1985.

Pecaut, M.J. & Mamajek, E.E., 2013. "Intrinsic Colors, Temperatures, and Bolometric Corrections of Pre-Main-Sequence Stars," *ApJS*, **208**, 9, Sept 2013.

Rogers, Christopher T., Ron Canterna, J. Allyn Smith, Michael J. Pierce, and Douglas L. Tucker, 2006. "Improved u′ g′ r′ i′ z′ to U B V Rc Ic Transformation Equations for Main-Sequence Stars," *The Astronomical Journal*, **132**, pp 989-993, September 2006.

Rowe, D., and Genet, R., 2015. "User's Guide to PS3 Speckle Interferometry Reduction Program," *Journal of Double Star Observations*, **11-1S**, 266, September 2015.

Rowe, D., 2017. "Guide to Using WDS1.2 Search Tool for the WDS Catalog," private communication, 2017.

Rowe, D., 2018. "Guide to GDS1.00 Gaia DR2 Double Star Catalog," private communication, July 17, 2018.

Rowe, D., 2020. "Speckle ToolBox 1.14 Bispectrum Data Reduction Tools," private communication presentation to Stanford On-Line High School students, June 26, 2020.

Tonry, J. L., L. Denneau, H. Flewelling, A. N. Heinze1, C. A. Onken, S. J. Smartt, B. Stalder, H. J. Weiland, C. Wolf, 2018. "The ATLAS All-Sky Stellar Reference Catalog," *The Astrophysical Journal*, **867**, 105, November 10, 2018.

Wasson, R., 2019. "Speckle Interferometry with the OCA Kuhn 22-in Telescope – II," *JDSO*, **15-2**, 273, April 2019.

Wasson, R., Genet, R., Rowe, D., 2021. "Speckle Photometry and Spectral Types of Close Binary Star Components," *Proceedings for the 40th Annual Symposium of the Society for Astronomical Sciences*, June 2021, 125-145.